# Microkinetic Molecular Volcano Plots for Enhanced Catalyst Selectivity and Activity Predictions

Thanapat Worakul,[||] Rubén Laplaza,[||] Shubhajit Das, Matthew D. Wodrich,* and Clemence Corminboeuf*

Cite This: ACS Catal. 2024, 14, 9829−9839

Read Online

ACCESS | Metrics & More | Article Recommendations | Supporting Information

**ABSTRACT:** Molecular volcano plots, which facilitate the rapid prediction of the activity and selectivity of prospective catalysts, have emerged as powerful tools for computational catalysis. Here, we integrate microkinetic modeling into the volcano plot framework to develop "microkinetic molecular volcano plots". The resulting unified computational framework allows the influence of important reaction parameters, including temperature, reaction time, and concentration, to be quickly incorporated and more complex situations, such as off-cycle resting states and coupled catalytic cycles, to be tackled. Compared to previous generations of molecular volcanoes, these microkinetic counterparts offer a more comprehensive understanding of catalytic behavior, in which selectivity and product ratios can be explicitly determined by tracking the evolution of each product concentration over time. This is demonstrated by examining two case studies, rhodium-catalyzed hydroformylation and metal-catalyzed hydrosilylation, in which the unique insights provided by microkinetic modeling, as well as the ability to simultaneously screen catalysts and reaction conditions, are highlighted. To facilitate the construction of these plots/maps, we introduce *mikimo*, a Python program that seamlessly integrates with our previously developed automated volcano builder, *volcanic*.

**KEYWORDS:** homogeneous catalysis, volcano plots, microkinetic modeling, hydroformylation, CO2 hydrosilylation
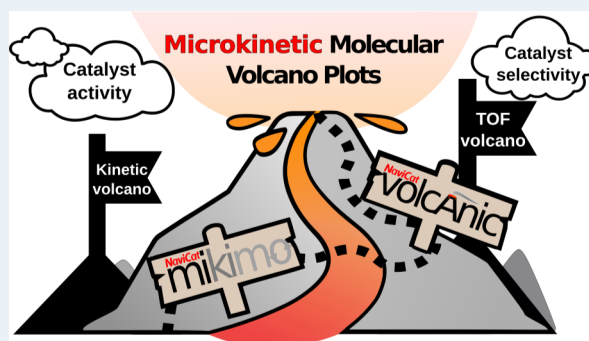


## INTRODUCTION

Volcano plots and related two-dimensional (2D) activity maps, built from linear free energy scaling relationships (LFESRs), have emerged as powerful tools for rationalizing and predicting catalytic properties.[1−5] Originally introduced in the context of heterogeneous (electro-)catalysis,[6−9] today molecular volcanoes[10−12] have found use in aspects of homogeneous catalysis ranging from smaller scale screening studies aimed at identifying ideal catalysts[13−15] to extracting overarching trends from catalyst space using larger data-driven workflows.[16−20] In essence, these plots/maps provide a quick assessment of the anticipated performance of prospective catalysts that traverse a catalytic cycle via a given reaction mechanism. Subsequent analysis allows optimal catalysts (which appear at the top of the volcano plot or in the most active region of the activity map) to be identified according to Sabatier's principle,[21] as well as global trends regarding catalyst behavior to be extracted.

Molecular volcano plots display the relationship between a measure of catalytic performance (on the $y$-axis) and a chosen descriptor variable (on the $x$-axis). While the latter is typically chosen to be the relative free energy of a selected catalytic cycle intermediate that is often determined through density functional theory (DFT) computations, numerous metrics of catalytic performance can be chosen for the former. Notably, this includes various measures of kinetic performance. The earliest variant defined catalytic activity in terms of a "kinetic determining step (kds)" (Figure 1a), which is the largest energy barrier between consecutive intermediates and transition states in the catalytic cycle (e.g., 1 → TS1, 2 → TS2).[11] This allowed rapid screening of catalysts, since only the value of the descriptor variable (which can be easily computed) is needed to estimate the kinetic performance of any prospective catalyst. However, such a simplified picture does not properly handle situations having multiple rate-determining steps nor does it accurately account for catalytic turnover. To improve upon this, we subsequently used the "energy span"[22−26] of the catalytic cycle to express kinetic performance in terms of a theoretically derived turnover frequency (TOF, Figure 1b).[12] Despite having recently been shown to capably estimate experimental catalytic perform-

**Figure 1.** Three generations of molecular volcano plots based on the different performance metrics: (a) Kinetic volcano plots (ref 11) based on the kinetic determining step $\Delta G(\text{kds})$, the barrier of the most energetically demanding step, (b) TOF volcano plots (ref 12) based on the theoretically determined turnover frequency, and (c) microkinetic volcano plots based on the product concentration at a given reaction time.



**Figure 2.** Modeling of homogeneous catalytic reactions. (a) Energy ($E$) representation. (b) General simulated reaction profile (SRP) that provides the free energy associated with moving between each set of linked species in the catalytic cycle (as indicated by the different colors) as a function of the descriptor variable. Plotted with a negative $y$-axis, the more positive steps (lowest-lying lines) delineate the kinetic volcano plot (shaded area). (c) Exemplary individual simulated reaction profiles corresponding to catalyst having descriptor variable values of **A** and **B** that are extracted from the general simulated reaction profile. TOF and microkinetic volcano plots are constructed by extracting numerous individual SRPs across a range of descriptor variable values. (d) Kinetic ($k$) representation, leading to a system of kinetic equations treated as an initial value problem.

ance[27,28] and representing the current state-of-the-art,[29−31] TOF volcanoes can only account for a single reaction pathway; they are unable to handle more complex situations involving competing or linked reaction pathways (e.g., situations where multiple products and/or regioisomers/enantiomers are possible).

Experimentally, key reaction properties, such as regio- and enantioselectivity, are determined by examining the distribu-

tion of products. On the other hand, computational treatments (including those obtained using volcano plots[32]) often rely on simple comparisons of the competing pathway energetics to estimate the final product ratio. While this may suffice to model selectivity trends (semiquantitatively),[33] accounting for off-cycle resting states, consecutive or coupled catalytic cycles, and/or potential conversions between pathways over time becomes tedious. Other, potentially important physical factors,

such as the influence of reactant concentration, cannot be described. Today, the most established approach for incorporating these effects into computational catalysis is through explicit microkinetic modeling (MKM).[33−43] This framework allows for a comprehensive analysis of complex reaction mechanisms that offers direct access to the evolution of product concentrations over time. To accomplish this, however, MKM first requires complete free energy profiles (often obtained through DFT computations) for each catalyst of interest, followed by solving a system of differential equations. The "computational bottleneck" associated with obtaining the required free energy profiles currently renders MKM impractical for the high-throughput analysis of hundreds or thousands of candidate catalysts.

In this work, the rapid screening ability of molecular volcano plots is combined with microkinetic modeling to create next-generation "microkinetic volcano plots and maps" that predict the concentration of the product(s) at a given reaction time (Figure 1c). Employing these two approaches in tandem enables both the catalyst and reaction conditions (temperature, time, and concentration) to be examined simultaneously, thereby providing quick access to quantitative selectivity trends. Here, we demonstrate the unique insights provided by these microkinetic volcanoes by analyzing two exemplary systems: transition-metal-catalyzed hydroformylation[11,32] and the stepwise hydrosilylation of $CO_2$.[33] To accompany this, we introduce *mikimo* (**mi**cro **ki**netic **mo**dule), a lightweight Python program that is seamlessly integrated with our previously released volcano plot/activity map builder, *volcanic*,[44] which automates the construction of microkinetic molecular volcano plots and activity/selectivity maps.

## METHODOLOGY

This section outlines the development of microkinetic molecular volcano plots beginning from DFT computed free energy profiles of catalytic reactions. More in-depth discussions on quantum chemical modeling of homogeneous catalytic reactions,[45−48] and a detailed protocol for building volcano plots (including for different types of molecular volcanoes) can be found elsewhere.[44] Readers interested only in the results obtained from the new maps/plots may skip directly to the Results and Discussion section.

**Theoretical Framework of Volcano Plots and Simulated Reaction Profiles (SRP).** Linear free energy scaling relationships (LFESRs) are the foundation on which molecular volcano plots are built. These equations relate the relative free energies of each catalytic cycle intermediate and transition state to one (or several) descriptor variable(s). The empirically derived linear fit is obtained by analyzing data from several different catalysts that follow the same reaction mechanism through the catalytic cycle. Note that poor fits are typically a result of different reaction mechanisms or specific interactions present within the set of catalysts considered (e.g., hydrogen bonds). Such situations usually demand the use of additional descriptor variables. A detailed discussion regarding the limitations of LFESRs and volcano plots can be found elsewhere.[44]

As an example, Figure 2a presents a representative free energy profile associated with a catalytic cycle. If the energy of **INT2** **R**elative to a selected **R**eference **S**tate (i.e., $\Delta G_{RRS}(INT2)$) is taken as the descriptor variable, the corresponding set of LFESRs can be written as follows:

$$\Delta G_{RRS}(Cat) = 0.0$$
$$\Delta G_{RRS}(INT1) = a_1 \Delta G_{RRS}(INT2) + c_1$$
$$\Delta G_{RRS}(TS1) = a_2 \Delta G_{RRS}(INT2) + c_2$$
$$\Delta G_{RRS}(INT2) = \Delta G_{RRS}(INT2)$$
$$\Delta G_{RRS}(TS2) = a_3 \Delta G_{RRS}(INT2) + c_3$$
$$\Delta G_{RRS}(Product) = \Delta G_{rxn} \tag{1}$$

The free energy associated with moving between directly linked intermediates and transition states can then be expressed as

$$\Delta G_{Cat \to INT1} = \Delta G_{RRS}(INT1) - \Delta G_{RRS}(Cat)$$
$$\Delta G_{INT1 \to TS1} = \Delta G_{RRS}(TS1) - \Delta G_{RRS}(INT1)$$
$$\Delta G_{TS1 \to INT2} = \Delta G_{RRS}(INT2) - \Delta G_{RRS}(TS1)$$
$$\Delta G_{INT2 \to TS2} = \Delta G_{RRS}(TS2) - \Delta G_{RRS}(INT2)$$
$$\Delta G_{TS2 \to Product} = -\Delta G_{rxn} - \Delta G_{RRS}(TS2) \tag{2}$$

Each of these equations can be rewritten by replacing the $\Delta G_{RRS}$ values in eq 2 with LFESRs found in eq 1. This yields a new set of equations that define a "simulated reaction profile (SRP)", in which the free energy associated with moving between each set of linked steps in the catalytic cycle can be expressed as a function of the descriptor variable, $\Delta G_{RRS}(INT2)$.

$$\Delta G_{Cat \to INT1} = a_1 \Delta G_{RRS}(INT2) + c_1$$
$$\Delta G_{INT1 \to TS1} = (a_2 - a_1) \Delta G_{RRS}(INT2) + c_2 - c_1$$
$$\Delta G_{TS1 \to INT2} = (1 - a_2) \Delta G_{RRS}(INT2) + c_2$$
$$\Delta G_{INT2 \to TS2} = (a_3 - 1) \Delta G_{RRS}(INT2) + c_3$$
$$\Delta G_{TS2 \to Product} = -\Delta G_{rxn} - a_3 \Delta G_{RRS}(INT2) + c_3 \tag{3}$$

Plotting these equations as a function of the descriptor variable (Figure 2b) not only gives the final volcano plot (i.e., the free energy associated with the most energetically costly reaction step, as indicated by the gray area in Figure 2b), but also defines a unique reaction profile associated with each value of the descriptor variable (e.g., the profiles of exemplary catalysts **A** and **B** are shown in Figure 2c).

**Microkinetic Modeling from Free Energy Profiles.** In catalytic reactions, each reaction step $i$ is characterized by a free energy barrier ($\Delta G_i^{\ddagger}$) that quantifies the energy difference between the TS and the preceding intermediate during the transformation. The relationship between $\Delta G_i^{\ddagger}$ and the rate constant $k_i$ is described by the Eyring–Polanyi equation (Figure 2d),[49] where $k_B$ is the Boltzmann constant, $h$ is the Planck constant, $R$ is the universal gas constant, $T$ is the temperature, and $\kappa$ is the transmission coefficient. Assuming $\kappa = 1$, the free energy associated with each elementary reaction step (as obtained from, for instance, the Figure 2a,c profiles) along with the reaction temperature can be used to calculate the corresponding forward and reverse rate constants (Figure 2d). A system of differential equations for all chemical species involved (catalysts, reactants, intermediates, and products) can then be constructed using these rate constants ($k_1 \cdots, k_n$) as coefficients, based on the proposed reaction mechanism.
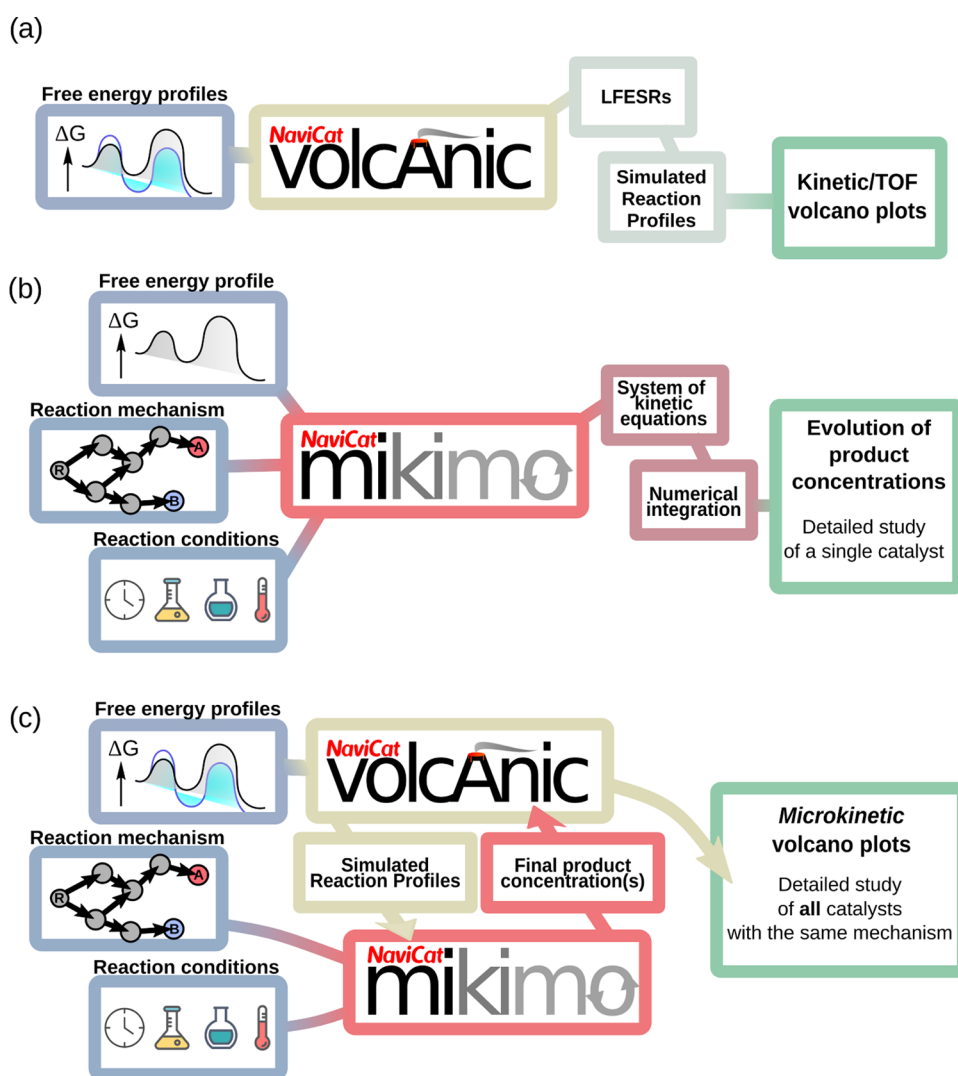
**Figure 3.** (a) Workflow of the *volcanic* program to generate kinetic or TOF volcano plots and activity maps from a set of free energy profiles, automatically generating the best possible LFESRs and the simulated reaction profiles. (b) Workflow of the *mikimo* program to perform microkinetic modeling of homogeneous catalytic reactions using a single free energy profile, reaction mechanism, and conditions. (c) Integration of *mikimo* and *volcanic* to yield microkinetic volcano plots. *mikimo* automatically performs microkinetic modeling in parallel using the simulated reaction profiles generated by *volcanic* from a set of free energy profiles.

Solving these equations through numerical integration yields the evolution of the concentration of each species over time.

**Microkinetic Volcano Plots.** For each possible value of the descriptor variable [e.g., $\Delta G_{RRS}(\text{INT2})$ in this example], estimates of the energy barriers associated with all of the individual reaction steps can be acquired from the general SRP (as demonstrated in Figure 2b,c). The corresponding rate constants can then be obtained for every reaction step from the Eyring–Polanyi equation and the kinetic equations constructed. The rate constants for the reverse reactions are obtained simultaneously and included in the preceding steps. For a given reaction time, the equations can then be integrated numerically, and the product concentration at a fixed time plotted as a function of the descriptor variable (for example, see Figure 1c). Since pathways leading to all possible products are included in both the reaction network and the kinetic equations, the concentration of several products or the ratio between products can be plotted, rather than a single concentration. Because the reaction pathways are coupled, the evolution of each product is affected by all other

transformations, which contrasts previous generations of molecular volcano plots in which each pathway was treated independently. Overall, this methodology can be applied to any reaction mechanism, irrespective of its complexity, because the reaction network (and the corresponding system of equations, Figure 2d) can capably describe any number of steps and connections between species.

Completing this process using a single descriptor variable gives rise to "microkinetic volcano plots", while using two descriptor variables (i.e., expressing the eq 1 LFESRs and the resulting SRPs as a function of two descriptor variables) provides "microkinetic activity maps". Importantly, for different values of the descriptor variable (or combinations of two descriptor variables), a system of kinetic equations can be constructed and integrated to obtain the product concentration. Thus, estimates of catalytic activity and selectivity are achieved by undertaking microkinetic modeling of only a handful of profiles corresponding to different descriptor values. This, coupled with the estimation (rather than computation) of the catalyst free energy profiles obtained from the SRPs,
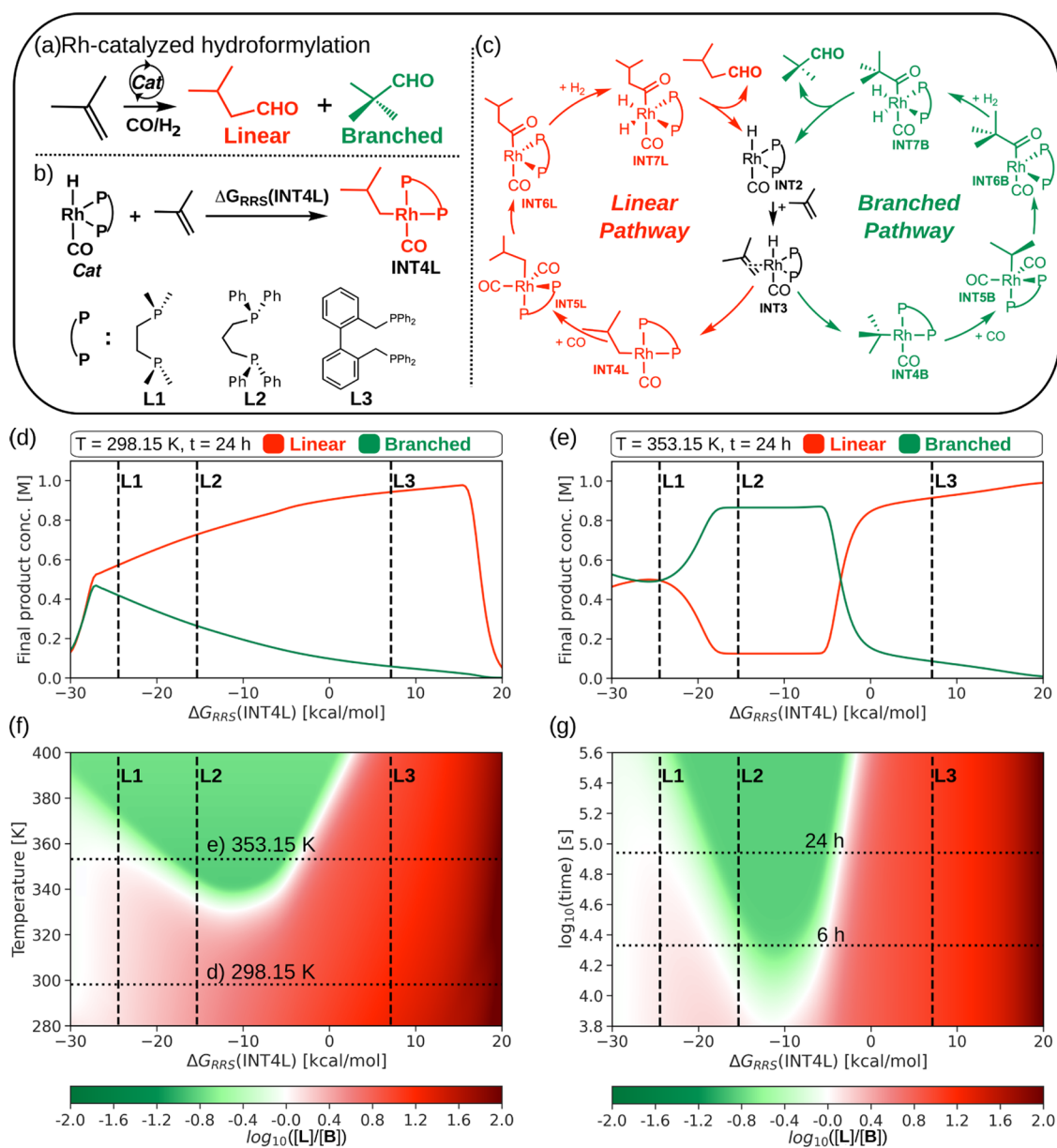
**Figure 4.** (a) Rh-catalyzed hydroformylation of an olefin showing linear (red) and branched (green) regioisomers. (b) Chemical equation used to determine the values of the descriptor variable, $\Delta G_{RRS}(INT4L)$. (c) Catalytic cycles leading to the formation of the potential products. (d) Microkinetic volcano plot with a reaction time of 24 h at 298.15 K. (e) Microkinetic volcano plot with a reaction time of 24 h at 353.15 K. (f) Microkinetic selectivity map displaying the influence of temperature on the final product distribution for a reaction time of 24 h. The dotted black lines indicate the location of (d) and (e) within the map. (g) Microkinetic selectivity map displaying the influence of reaction time on the final product distribution for a reaction at 353.15 K. The initial reactant concentrations are 1 M for CO, $H_2$, and 2-methylprop-1-ene, and 0.01 M for the Rh catalyst. Original data taken from ref 32.

results in considerable time savings relative to the computation and subsequent MKM of individual catalysts by hand.

Constructing microkinetic volcano plots/activity maps requires the following elements: (i) a number of free energy profiles to establish LFESRs (as in previous generations of volcano plots), (ii) a reaction mechanism where stationary points are connected through transition states (to establish rate constants), and (iii) the reaction conditions (initial concentrations, time and temperature), which are used to compute the rate constants and construct the system of kinetic equations to be solved for different values of the descriptor variable.

**Automated Construction of Microkinetic Volcano Plots and Activity Maps Using *mikimo* and *volcanic*.** Our previously developed *volcanic* software is able to read a file with the relative free energies of all species in the catalytic cycle for a set of catalysts, build all possible LFESRs, and select the best one. If the user agrees, *volcanic* constructs the SRP using the chosen descriptor variable, from which kinetic and TOF volcano plots are readily built (Figure 3a).[44] To extend its capabilities to microkinetic volcano plots and activity maps, we developed the *mikimo* (**mi**cro **ki**netic **mo**dule) program, which can be used in a standalone form or in tandem with *volcanic*.

*mikimo* performs explicit simulations by reading a computed free energy profile, a user-defined reaction mechanism that

specifies the reaction network (i.e., the interconnectivity between intermediates and transition states), as well as all relevant experimental conditions (i.e., temperature, time, and initial concentrations of the reactants), as overviewed in Figure 3b. The system of kinetic equations, along with the initial concentration input for all species, is numerically integrated using the initial value problem solver implemented in the *Scipy* library,[50] using automatic differentiation implemented in Autograd library[51] to compute the Jacobian matrix. The resulting MKM simulation then provides detailed information about how the concentration of species evolves over the course of a reaction for a single catalyst.

When used with *volcanic*, *mikimo* processes the simulated reaction profiles (SRPs, *vide supra*) provided by *volcanic* to generate microkinetic volcano plots and activity maps (Figure 3c). To accelerate the integration of many systems of differential equations, our implementation evaluates a subset of SRPs in parallel and interpolates the results to cover the desired range of descriptor variables. Savitzky-Golay[52] and Wiener[53] filters have been implemented to ensure smooth interpolation. Similar to *volcanic*, the required input of *mikimo* is one (or more) computed free energy profiles and a flexible reaction network specification (e.g., through a CSV file). The open-source software and user instructions are available at https://github.com/lcmd-epfl/mikimo/.

## ■ RESULTS AND DISCUSSION

With the theoretical framework and the implementation of microkinetic volcano plots in hand, we now demonstrate their application for two different catalytic reactions. Owing to their ability to account for temperature and concentration in complex mechanisms, microkinetic activity maps that use time or temperature as secondary descriptors allow for the simultaneous optimization of both catalyst and reaction conditions.

**Regioselectivity in Rh-Catalyzed Hydroformylation.** Hydroformylation is an industrially important transition-metal-catalyzed process that converts olefins, CO, and $H_2$ into linear and branched aldehydes.[54] Previously, we screened rhodium bisphosphine catalysts based on activity and regioselectivity in the hydroformylation of 1,1-dimethylethylene to form either a linear (**L**) or a branched (**B**) product (see catalytic cycle, Figure 4a).[32] A volcano plot constructed using $\Delta G_{RRS}(INT4L)$ (as defined in Figure 4b) as the descriptor variable revealed that the **L** pathway is kinetically more favorable than the **B** pathway (Figure 4c and Supporting Information, SI Figure S2a). However, previously we could only assess each pathway independently, which neglected the coupled nature of the cycles. Figure 4d shows a microkinetic volcano plot generated at 298.15 K after 24 h of simulated reaction time, in which the final concentration of products **L** and **B** is obtained through explicit microkinetic modeling of the entire reaction network. The region of maximum activity, as reflected by the total concentration of all products produced during the reaction approaching 1 M, is associated with descriptor variable values (plotted on the *x*-axis) lying between −28 and +16 kcal/mol. In all cases, preferential formation of the **L** over **B** product is observed, as indicated by the red line (associated with the **L** product) lying above the green line (associated with the **B** product) on the plot. Regioselectivity toward the **L** product increases toward the right side of the volcano, as shown by the growing gap between the red and green lines in Figure 4d. Examining some of our previously computed pool of candidate

ligands, **L1** $[\Delta G_{RRS}(INT4L) = -24.45$ kcal/mol$]$, was found to be significantly less selective $([\mathbf{L}]:[\mathbf{B}] = 1.4:1)$ than the large, aryl-containing **L3** ligand $[\Delta G_{RRS}(INT4L) = 7.13$ kcal/mol$]$ at 298.15 K $([\mathbf{L}]:[\mathbf{B}] = 16.2:1)$. An extended pool of ligands is presented in SI Figure S6.

Using microkinetic volcano plots, we are easily able to examine the same reaction at a higher temperature of 353.15 K (Figure 4e). Here, a shift in the dominant product from **L** (at 298.15 K) to **B** (at 353.15 K) is seen for values of the descriptor variable between −30 and −5 kcal/mol (red pathway preferred in Figure 4d and green pathway in Figure 4e). This reversal of preferred product occurs because the energy barriers and elementary reaction energies of the **L** pathway are low enough that the linear product undergoes reverse reactions and enters the **B** pathway. Ultimately, the thermodynamically more stable branched regiomer is produced with longer reaction time and/or higher temperatures. This chameleonic shift in the dominant product at higher temperatures is exemplified by **L2** $[\Delta G_{RRS}(INT4L) = -15.35$ kcal/mol$]$ which is highly active and selective for the branched product **B** at 353.15 K (Figure 4e, $([\mathbf{B}]:[\mathbf{L}] = 6.9:1))$ while being relatively selective for the linear product **L** at 298.15 K $([\mathbf{L}]:[\mathbf{B}] = 2.8:1,$ Figure 4d). Experimentally, **L2** has been shown to favor **B** over **L** (albeit with a different substrate) with high temperature and long reaction times,[55,56] while **L3** is known to favor the linear product even under harsh conditions,[57,58] in agreement with the results from our microkinetic volcano plots $([\mathbf{L}]:[\mathbf{B}] = 10.6:1)$. Importantly, behavior of this type cannot be easily discerned using previous generations of molecular volcano plots where the two cycles are treated independently (see Figure S1 for a comparison).

To provide a more comprehensive analysis of the influence of reaction time and temperature on regioselectivity, microkinetic selectivity maps, as shown in Figure 4f,g, can be constructed. Here, the ratio of the product concentrations $[\mathbf{L}]$ and $[\mathbf{B}]$ (in logarithmic scale, color axis) is plotted as a function of the original descriptor variable used in the previous volcano plots, $\Delta G_{RRS}(INT4L)$ (*x*-axis), and either the temperature or reaction time (*y*-axis).[59] As shown in Figure 4f, at a reaction time of 24 h **L** is favored over **B** under mild conditions (temperature <320 K), as also seen in Figure 4b. At $T \approx 340$ K, a change of preferred regioisomer is first observed, but only for catalysts lying in a very narrow range of descriptor variable $[\Delta G_{RRS}(INT4L) \approx -10$ kcal/mol$]$. Increasing the temperature further leads not only to a higher proportion of the branched isomer in the product distribution but also to a larger number of catalysts exhibiting this behavior (i.e., significantly more catalysts will have descriptor values lying between −30 and −5 kcal/mol than those having values of −10 kcal/mol). Conversely, catalysts having descriptor variables with values >5 kcal/mol should preferentially produce the **L** regioisomer at any temperature.

Reaction time has a similar effect to increasing reaction temperature on the product ratio that highlights the thermodynamic control of the reaction (Figure 4g). As the time of the reaction increases, the range of descriptor values in which the branched isomer predominates also increases. Overall, rhodium catalysts possessing exergonic $\Delta G_{RRS}(INT4L)$ values should exhibit a preference toward the branched regioisomer, given adequately long reaction times and a temperature over 320 K (see SI Figure S3). Such examples indicate that the use of bisphosphine ligands featuring alkyl linkers (in particular, propyl- and butyl-, see
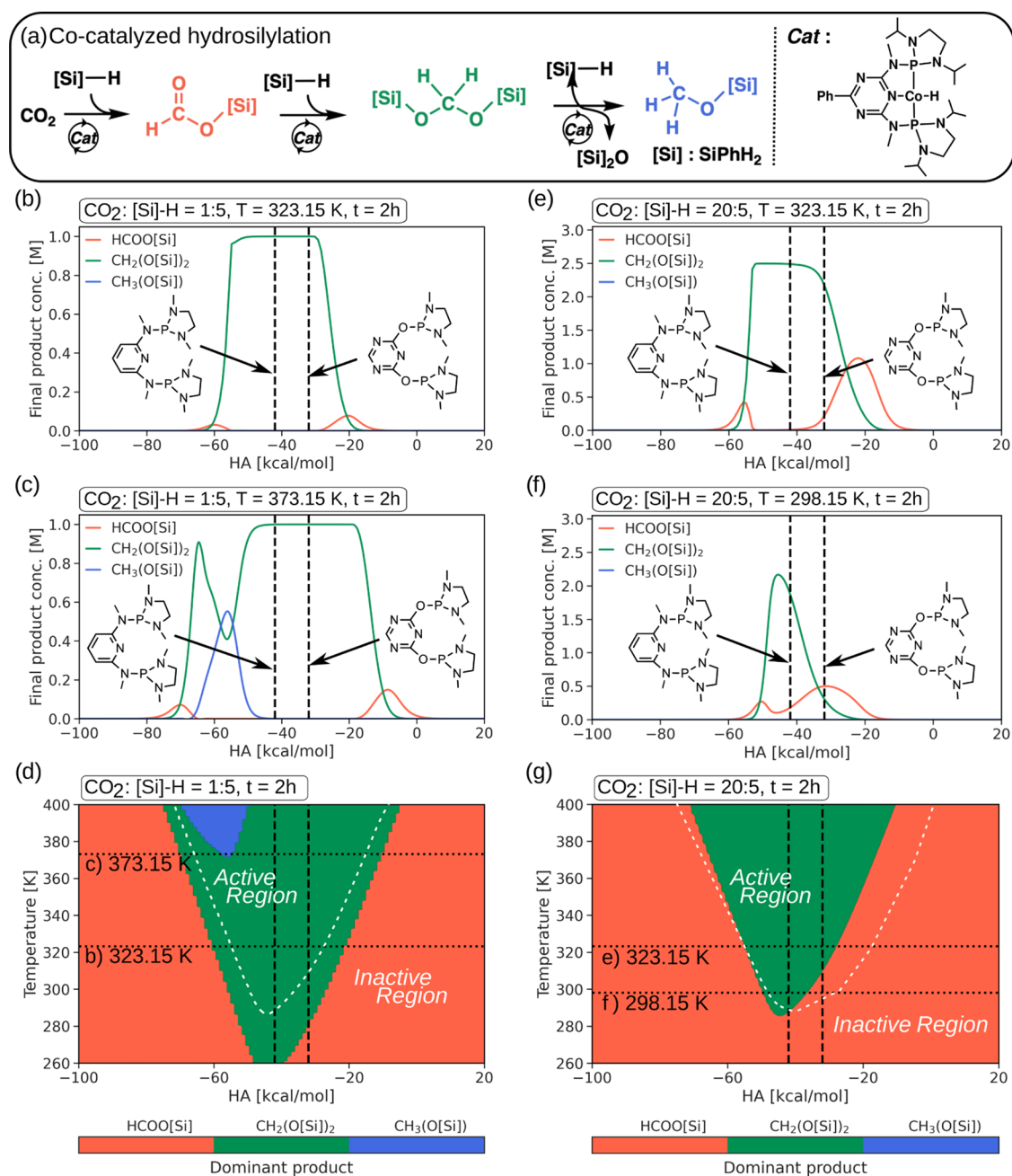
**Figure 5.** (a) Simplified reaction mechanism for the stepwise catalytic reduction of $CO_2$ to formate, acetal, and methoxide products. (b, c) Chemoselective microkinetic volcano plots at 323.15 and 373.15 K. Initial concentrations are 0.05 M (catalyst), 1 M ($CO_2$), and 5 M (silane). (d) Microkinetic map describing selectivity as a function of HA and temperature. The initial reactant concentrations are 5 M (silane) and 0.05 M (catalyst), with a reaction time of 2 h. The active region, corresponding to appreciable catalytic turnover, is enclosed by the white dashed line. Black dotted lines indicate the location of panels b and c within the map, while the dashed black lines indicate the position of the catalysts shown in (b) and (c). (e, f) Chemoselective microkinetic volcano plots at 323.15 and 298.15 K. Initial concentrations are 0.05 M (catalyst), 20 M ($CO_2$), and 5 M (silane). (g) Microkinetic map describing selectivity as a function of HA and temperature. Initial reactant concentrations are 5 M (silane) and 0.05 M (catalyst), with a reaction time of 2 h. The active region is enclosed by the white dashed line. The black dotted lines indicate the location of (e) and (f) within the map, while the dashed black lines indicate the position of the catalysts shown in (e) and (f). Original DFT data was taken from ref 28, and the relevant catalytic cycle is shown in SI Figure S13.

SI Figure S6) may represent a route toward "rule breaking" catalyst that selectively forms tertiary aldehydes in violation of Keulemans' law.[60] Ligands in which $\Delta G_{RRS}$(INT4L) is only slightly exergonic, such as DIOP and PhanePhos, require increasingly high temperatures and time scales to reverse their selectivity (SI Figure S6).

Overall, this example demonstrates how microkinetic volcano plots and activity maps lead to a quantitative

understanding of regioselectivity reversal that arises through the competition between kinetically and thermodynamically preferred pathways. The temperature and time threshold where a switch of preferred regioisomer from **L** to **B** takes place can be quickly estimated for any potential catalyst simply from knowledge of the descriptor variable.

**Catalytic Hydrosilylation of $CO_2$ with Metal Pincer Complexes.** As a second illustration of the power of

microkinetic volcano plots, we demonstrate their ability to describe selectivity in complex reaction mechanisms featuring intertwined catalytic cycles. Recently, the hydride affinity (HA) of transition metal pincer complexes was linked to catalytic activity and selectivity in consecutive hydrosilylation reactions of $CO_2$ to produce silyl formate ($HCOO[Si]$), bis(silyl)acetal ($CH_2(O[Si])_2$), or methoxysilanes ($CH_3(O[Si])$) where $[Si]$ = $SiPhH_2$.[28] HA was estimated from the free energy change of eq 4, providing a direct measure of the intrinsic acidity of the metal center.[28,33]

$$\text{HA} = (\Delta G_{[[M]-H]^+} + \Delta G_{Ph_3CH}) - (\Delta G_{[M]} + \Delta G_{[Ph_3C]^+}) \tag{4}$$

Catalytic hydrosilylation proceeds via three sequential cycles corresponding to $2e^-$, $4e^-$, and $6e^-$ reductions of the substrate (Figure 5a). The complexity and intertwined nature of these catalytic cycles previously prevented us from creating a unified volcano plot able to quantitatively predict the product distribution. Instead, we developed a composite volcano picture by superimposing the three individual volcano plots that corresponded to each of the three cycles, which led to a semiquantitative description of the observed selectivity.[28] Now, using microkinetic volcano plots (based on DFT data from our previous work[33]), we are able to obtain the previously inaccessible unified description of activity and selectivity that considers the complete catalytic process together.

Ideally, one would like to have full control over the catalytic cycle such that any of the three potential reduction products (i.e., orange, green, blue in Figure 5a) could be favored through alternation of a combination of the catalyst, concentration of the reactants, and reaction temperature. As an initial set of conditions, we analyzed a reaction proceeding for 2 h at 323.15 K with a $CO_2$ to $[Si]-H$ ratio of 1:5. Under such conditions, $CH_2(O[Si])_2$ is the dominant product (green line, Figure 5b) for any catalyst having a descriptor variable values between −60 and −20 kcal/mol, including the two exemplary (PNP and PONOP) ligands indicated by vertical dashed lines. For a very narrow range of catalysts lying between −20 and −10 kcal/mol, $HCOO[Si]$ is the major product (red line, Figure 5b); however, such catalysts are expected to behave sluggishly, as indicated by the low concentration of product obtained after the 2 h reaction time. Overall, under such reaction conditions, it is clear that $HCOO[Si]$ does not accumulate, instead proceeding quickly into the second cycle and forming the more thermodynamically favored $CH_2(O[Si])_2$ product.

This situation, however, changes for longer reaction times and higher temperatures (373.15 K), where $CH_3(O[Si])$ emerges as a product for catalysts in the −75 < HA < −47 kcal/mol range (Figure 5c), aligning with the peak of the TOF volcano plot for the third cycle (SI Figure S10). This descriptor variable range corresponds to strongly donating ligands that would possess large negative HA values. However, creating ligands of this type is difficult, as evidenced by a lack of species possessing these properties in the original database.[28] In parallel to the effect of temperature, the top region of $CH_3(O[Si])$ continues to rise and also broadens as reaction time increases (SI Figures S11 and S12), which would allow certain catalysts (i.e., those having descriptor values in the −70 to −45 range) to completely reduce $CO_2$ given sufficient time and temperature.

On the other hand, altering the $CO_2$:$[Si]$-H ratio to 20:5 (from 1:5) can be used to stop the reaction earlier. Figure 5e

shows a substantial increase in the maximum concentration of $HCOO[Si]$ in the −40 < HA < − 5 kcal/mol region, where the TOF of the first reaction is highest (SI Figure S10). By lowering the reaction temperature from 323.15 to 298.15 K, the system becomes dominated by reaction kinetics (as opposed to thermodynamics), which allows formate to become the dominant product for triazine PONOP pincer catalysts (Figure 5f). Naturally, lowering the temperature has an accompanying depressing effect on catalytic activity. As illustrated by these microkinetic volcano plots, $CO_2$ pressure, temperature, and catalyst choice are all crucial handles to control product distribution. We note that a $CO_2$ concentration of 20 M may be unattainable within the pressure ranges of typical laboratory setups. However, the overall effect of increasing the $CO_2$ pressure is similar, albeit less marked, at lower concentrations (see SI Figure S14).

Microkinetic activity maps more clearly illustrate the interplay between changes in the catalyst (monitored by the descriptor variable, HA, in this example) and reaction conditions. Plotting temperature on the y-axis (Figure 5d) shows how the active region of the map is dominated by $CH_2(O[Si])_2$ (green) at lower temperatures (e.g., for the bottom dashed horizontal line at 323.15 K). Increasing the temperature, however, allows $CH_3(O[Si])$(blue) to become the primary product, at first for only a very narrow range of catalysts (e.g., for the top dashed horizontal line at 373.15 K) but only for a narrow (albeit increasingly larger as the temperature is increased) range of catalysts.

Increasing the concentration of $CO_2$ leads to an overall increase in the size of the active region (the area enclosed by the white dashed line in Figure 5g compared to Figure 5d), which now allows production of either $CH_2(O[Si])_2$ (green) or $HCOO[Si]$(red) at 323.15 K (upper dashed horizontal line), depending on the nature of the catalyst. However, finding a catalyst with descriptor variable values lying in the narrow orange bands at the periphery of the active region may be difficult. By lowering the reaction temperature (to 298.15 K, lower dashed horizontal line), the types of catalysts that preferentially form the $HCOO[Si]$ product change, as illustrated for the PONOP catalyst in Figure 5e,f. It should be noted, however, that no product is formed at temperatures below 280 K. Thus, the preferred products can be manipulated through a change of temperature, but there are likely upper (e.g., where the catalyst dissociates) and lower bounds (e.g., where there is insufficient energy for the reaction to take place) to this strategy.

## ■ CONCLUSIONS

We have introduced microkinetic volcano plots and activity/selectivity maps, which extend the capabilities of previous variants of molecular volcano plots/maps. Specifically, these new plots enable not only rapid catalyst screening for reactions involving complicated mechanisms (e.g., intertwined catalytic cycles leading to multiple products) but also the effect of physical conditions (e.g., reaction temperature/length, concentration of reactants) on activity and selectivity. Leveraging these capabilities permits the simultaneous optimization of the catalyst and the reaction conditions, thereby providing a unified theoretical framework for the holistic design of active and selective homogeneous catalysts and reactions. To facilitate construction of these plots/maps, we have introduced *mikimo*, a Python-based open-source module for microkinetic modeling of homogeneous catalytic reactions (see data

availability statement for links). This easy-to-use implementation predicts product distributions in line with experimental observations, and is applicable to diverse reaction mechanisms as well as conditions. The utility of both the underlying conceptual tools and the program has been demonstrated through the study of rhodium-catalyzed hydroformylation and cobalt-catalyzed hydrosilylation reactions. We hope these new tools will be beneficial to the broader catalysis community.

## ■ COMPUTATIONAL DETAILS

Free energy profiles used to construct LFESRs and the microkinetic volcano plots/activity maps were obtained from density functional theory computations taken from previous works.[28,32,33] For the rhodium-catalyzed hydroformylation, computations were performed at the PBE0-dDsC[61−66]/TZ2P//M06[67]/def2-SVP[68] level of theory using Gaussian09[69] for geometry optimization/frequencies and ADF[70,71] for final single point electronic energies including COSMO-RS solvation corrections[72] in benzene. The catalytic hydrosilylation example used SMD$_{benzene}$/M06/def2-TZVP[73]//M06/def2-SVPD level computations in Gaussian16.[74] Further details can be found in the original publications (ref 32 for hydroformylation and ref 28 for hydrosilylation).

## ■ ASSOCIATED CONTENT

### Data Availability Statement
Data used to produce the volcano plots and activity/selectivity maps in this study, along with the user instructions for their automated construction using *mikimo*, are available at https://github.com/lcmd-epfl/mikimo/examples and https://github.com/lcmd-epfl/mikimo/test_cases. The package can be found at https://github.com/lcmd-epfl/mikimo.

### ⓢ Supporting Information
The Supporting Information is available free of charge at https://pubs.acs.org/doi/10.1021/acscatal.4c01175.

> Confidence and prediction intervals for the Rh-catalyzed hydroformylation microkinetic volcano plots; additional volcano plots and microkinetic simulations for the Rh-catalyzed hydroformylation reaction; correlation plots between free energy corrections; TOF-based selectivity map; complete list of ligands; free energy profiles; validation on an extrapolated catalyst; microkinetic study of the catalytic hydrosilylation reaction; TOF and microkinetic volcano plots and activity maps for the hydrosilylation reaction; and catalytic cycle for the hydrosilylation reaction (PDF)

## ■ AUTHOR INFORMATION

### Corresponding Authors
**Matthew D. Wodrich** − *Laboratory for Computational Molecular Design, Institute of Chemical Sciences and Engineering, Ecole Polytechnique Fedéralé de Lausanne (EPFL), 1015 Lausanne, Switzerland; National Center for Competence in Research-Catalysis (NCCR-Catalysis), Ecole Polytechnique Fédéralé de Lausanne (EPFL), 1015 Lausanne, Switzerland;* orcid.org/0000-0002-6006-671X; Email: matthew.wodrich@epfl.ch
**Clemence Corminboeuf** − *Laboratory for Computational Molecular Design, Institute of Chemical Sciences and Engineering, Ecole Polytechnique Fedéralé de Lausanne (EPFL), 1015 Lausanne, Switzerland; National Center for Competence in Research-Catalysis (NCCR-Catalysis), Ecole Polytechnique Fédérale de Lausanne (EPFL), 1015 Lausanne, Switzerland;* orcid.org/0000-0001-7993-2879; Email: clemence.corminboeuf@epfl.ch

### Authors
**Thanapat Worakul** − *Laboratory for Computational Molecular Design, Institute of Chemical Sciences and Engineering, Ecole Polytechnique Fedéralé de Lausanne (EPFL), 1015 Lausanne, Switzerland;* orcid.org/0000-0002-8031-1727
**Rubén Laplaza** − *Laboratory for Computational Molecular Design, Institute of Chemical Sciences and Engineering, Ecole Polytechnique Fedéralé de Lausanne (EPFL), 1015 Lausanne, Switzerland; National Center for Competence in Research-Catalysis (NCCR-Catalysis), Ecole Polytechnique Fédéralé de Lausanne (EPFL), 1015 Lausanne, Switzerland;* orcid.org/0000-0001-6315-4398
**Shubhajit Das** − *Laboratory for Computational Molecular Design, Institute of Chemical Sciences and Engineering, Ecole Polytechnique Fedéralé de Lausanne (EPFL), 1015 Lausanne, Switzerland; Present Address: Faculty of Chemistry and Food Chemistry, Technische Universität Dresden, 01062 Dresden, Germany;* orcid.org/0000-0002-8027-6781

Complete contact information is available at:
https://pubs.acs.org/10.1021/acscatal.4c01175

### Author Contributions
∥T.W. and R.L. contributed equally to this work.

### Notes
The authors declare no competing financial interest.

## ■ ACKNOWLEDGMENTS

## ■ REFERENCES

(1) Nørskov, J. K.; Bligaard, T.; Rosmeisl, J.; Christensen, C. H. Towards the computational design of solid catalysts. *Nat. Chem.* **2009**, *1*, 37−46.
(2) Exner, K. S. Importance of the volcano slope to comprehend activity and selectivity trends in electrocatalysis. *Curr. Opin. Electrochem.* **2023**, *39*, 101284.
(3) Wodrich, M. D.; Sawatlon, B.; Busch, M.; Corminboeuf, C. The Genesis of Molecular Volcano Plots. *Acc. Chem. Res.* **2021**, *54*, 1107−1117.
(4) Anand, M.; Rohr, B.; Statt, M. J.; Nørskov, J. K. Scaling Relationships and Volcano Plots in Homogeneous Catalysis. *J. Phys. Chem. Lett.* **2020**, *11*, 8518−8526.
(5) Yang, L.-C.; Hong, X. Scaling relationships and volcano plots of homogeneous transition metal catalysis. *Dalton Trans.* **2020**, *49*, 3652−3657.
(6) Cheng, J.; Hu, P.; Ellis, P.; French, S.; Kelly, G.; Lok, C. M. Brønsted-Evans-Polanyi Relation of Multistep Reactions and Volcano Curve in Heterogeneous Catalysis. *J. Phys. Chem. C* **2008**, *112*, 1308−1311.
(7) Nørskov, J. K.; Rossmeisl, J.; Logadottir, A.; Lindqvist, L.; Kitchin, J. R.; Bligaard, T.; Jónsson, H. Origin of the Overpotential for

Oxygen Reduction at a Fuel-Cell Cathode. *J. Phys. Chem. B* **2004**, *108*, 17886−17892.

(8) Nørskov, J. K.; Bligaard, T.; Logadottir, A.; Kitchin, J. R.; Chen, J. G.; Pandelov, S.; Stimming, U. Trends in the Exchange Current for Hydrogen Evolution. *J. Electrochem. Soc.* **2005**, *152*, J23.

(9) Medford, A. J.; Vojvodic, A.; Hummelshøj, J. S.; Voss, J.; Abild-Pedersen, F.; Studt, F.; Bligaard, T.; Nilsson, A.; Nørskov, J. K. From the Sabatier principle to a predictive theory of transition-metal heterogeneous catalysis. *J. Catal.* **2015**, *328*, 36−42.

(10) Busch, M.; Wodrich, M. D.; Corminboeuf, C. Linear scaling relationships and volcano plots in homogeneous catalysis—revisiting the Suzuki reaction. *Chem. Sci.* **2015**, *6*, 6754−6761.

(11) Wodrich, M. D.; Busch, M.; Corminboeuf, C. Accessing and predicting the kinetic profiles of homogeneous catalysts from volcano plots. *Chem. Sci.* **2016**, *7*, 5723−5735.

(12) Wodrich, M. D.; Sawatlon, B.; Solel, E.; Kozuch, S.; Corminboeuf, C. Activity-Based Screening of Homogeneous Catalysts through the Rapid Assessment of Theoretically Derived Turnover Frequencies. *ACS Catal.* **2019**, *9*, 5716−5725.

(13) Sawatlon, B.; Wodrich, M. D.; Corminboeuf, C. Unraveling Metal/Pincer Ligand Effects in the Catalytic Hydrogenation of Carbon Dioxide to Formate. *Organometallics* **2018**, *37*, 4568−4575.

(14) Anand, M.; Nørskov, J. K. Scaling Relations in Homogeneous Catalysis: Analyzing the Buchwald-Hartwig Amination Reaction. *ACS Catal.* **2020**, *10*, 336−345.

(15) Wodrich, M. D.; Corminboeuf, C. Methoxycyclization of 1,5-Enynes by Coinage Metal Catalysts: Is Gold Always Superior? *Helv. Chim. Acta* **2021**, *104*, No. e2100134.

(16) Busch, M.; Wodrich, M. D.; Corminboeuf, C. A Generalized Picture of C-C Cross-Coupling. *ACS Catal.* **2017**, *7*, 5643−5653.

(17) Meyer, B.; Sawatlon, B.; Heinen, S.; von Lilienfeld, O. A.; Corminboeuf, C. Machine learning meets volcano plots: computational discovery of cross-coupling catalysts. *Chem. Sci.* **2018**, *9*, 7069−7077.

(18) Sawatlon, B.; Wodrich, M. D.; Meyer, B.; Fabrizio, A.; Corminboeuf, C. Data Mining the C-C Cross-Coupling Genome. *ChemCatChem* **2019**, *11*, 4096−4107.

(19) Wodrich, M. D.; Fabrizio, A.; Meyer, B.; Corminboeuf, C. Data-powered augmented volcano plots for homogeneous catalysis. *Chem. Sci.* **2020**, *11*, 12070−12080.

(20) Cordova, M.; Wodrich, M. D.; Meyer, B.; Sawatlon, B.; Corminboeuf, C. Data-Driven Advancement of Homogeneous Nickel Catalyst Activity for Aryl Ether Cleavage. *ACS Catal.* **2020**, *10*, 7021−7031.

(21) Sabatier, P. Hydrogénations et déshydrogénations par catalyse. *Ber. Dtsch. Chem. Ges.* **1911**, *44*, 1984−2001.

(22) Kozuch, S.; Shaik, S. Kinetic-Quantum Chemical Model for Catalytic Cycles: The Haber-Bosch Process and the Effect of Reagent Concentration. *J. Phys. Chem. A* **2008**, *112*, 6032−6041.

(23) Kozuch, S.; Shaik, S. How to Conceptualize Catalytic Cycles? The Energetic Span Model. *Acc. Chem. Res.* **2011**, *44*, 101−110.

(24) Kozuch, S. A refinement of everyday thinking: the energetic span model for kinetic assessment of catalytic cycles. *Wiley Interdiscip. Rev.: Comput. Mol. Sci.* **2012**, *2*, 795−815.

(25) Garay-Ruiz, D.; Bo, C. Revisiting Catalytic Cycles: A Broader View through the Energy Span Model. *ACS Catal.* **2020**, *10*, 12627−12635.

(26) Laplaza, R.; Gallarati, S.; Corminboeuf, C. Genetic Optimization of Homogeneous Catalysts. *Chem. Methods* **2022**, *2*, No. e202100107.

(27) Das, S.; Turnell-Ritson, R. C.; Dyson, P. J.; Corminboeuf, C. Design of Frustrated Lewis Pair Catalysts for Direct Hydrogenation of CO₂. *Angew. Chem., Int. Ed.* **2022**, *61*, No. e202208987.

(28) Cramer, H. H.; Das, S.; Wodrich, M. D.; Corminboeuf, C.; Werlé, C.; Leitner, W. Theory-guided development of homogeneous catalysts for the reduction of CO₂ to formate, formaldehyde, and methanol derivatives. *Chem. Sci.* **2023**, *14*, 2799−2807.

(29) Sawatlon, B.; Wodrich, M. D.; Corminboeuf, C. Probing Substrate Scope with Molecular Volcanoes. *Org. Lett.* **2020**, *22*, 7936−7941.

(30) Das, S.; Laplaza, R.; Blaskovits, J. T.; Corminboeuf, C. Mapping Active Site Geometry to Activity in Immobilized Frustrated Lewis Pair Catalysts. *Angew. Chem., Int. Ed.* **2022**, *61*, No. e202202727.

(31) Gallarati, S.; Laplaza, R.; Corminboeuf, C. Harvesting the fragment-based nature of bifunctional organocatalysts to enhance their activity. *Org. Chem. Front.* **2022**, *9*, 4041−4051.

(32) Wodrich, M. D.; Busch, M.; Corminboeuf, C. Expedited Screening of Active and Regioselective Catalysts for the Hydroformylation Reaction. *Helv. Chim. Acta* **2018**, *101*, No. e1800107.

(33) Cramer, H. H.; Ye, S.; Neese, F.; Werlé, C.; Leitner, W. Cobalt-Catalyzed Hydrosilylation of Carbon Dioxide to the Formic Acid, Formaldehyde, and Methanol Level—How to Control the Catalytic Network? *JACS Au* **2021**, *1*, 2058−2069.

(34) Rush, L. E.; Pringle, P. G.; Harvey, J. N. Computational Kinetics of Cobalt-Catalyzed Alkene Hydroformylation. *Angew. Chem., Int. Ed.* **2014**, *53*, 8672−8676.

(35) Wodrich, M. D.; Ye, B.; Gonthier, J. F.; Corminboeuf, C.; Cramer, N. Ligand-Controlled Regiodivergent Pathways of Rhodium-(III)-Catalyzed Dihydroisoquinolone Synthesis: Experimental and Computational Studies of Different Cyclopentadienyl Ligands. *Chem. - Eur. J.* **2014**, *20*, 15409−15418.

(36) Besora, M.; Maseras, F. Microkinetic modeling in homogeneous catalysis. *Wiley Interdiscip. Rev.: Comput. Mol. Sci.* **2018**, *8*, e1372.

(37) Besora, M.; Braga, A. A. C.; Sameera, W. M. C.; Urbano, J.; Fructos, M. R.; Pérez, P. J.; Maseras, F. A computational view on the reactions of hydrocarbons with coinage metal complexes. *J. Organomet. Chem.* **2015**, *784*, 2−12.

(38) Wei, D.; Roisnel, T.; Darcel, C.; Clot, E.; Sortais, J.-B. Hydrogenation of Carbonyl Derivatives with a Well-Defined Rhenium Precatalyst. *ChemCatChem* **2017**, *9*, 80−83.

(39) Heitkämper, J.; Herrmann, J.; Titze, M.; Bauch, S. M.; Peters, R.; Kästner, J. Asymmetric Hydroboration of Ketones by Cooperative Lewis Acid-Onium Salt Catalysis: A Quantum Chemical and Microkinetic Study to Combine Theory and Experiment. *ACS Catal.* **2022**, *12*, 1497−1507.

(40) Ishikawa, A.; Tateyama, Y. A First-Principles Microkinetics for Homogeneous−Heterogeneous Reactions: Application to Oxidative Coupling of Methane Catalyzed by Magnesium Oxide. *ACS Catal.* **2021**, *11*, 2691−2700.

(41) Li, Q.; García-Muelas, R.; López, N. Microkinetics of alcohol reforming for H₂ production from a FAIR density functional theory database. *Nat. Commun.* **2018**, *9*, No. 526.

(42) Sciortino, G.; Maseras, F. Microkinetic modelling in computational homogeneous catalysis and beyond. *Theor. Chem. Acc.* **2023**, *142*, 99.

(43) Sabadell-Rendón, A.; Kaźmierczak, K.; Morandi, S.; Euzenat, F.; Curulla-Ferré, D.; López, N. Automated MUltiscale simulation environment. *Digital Discovery* **2023**, *2*, 1721−1732.

(44) Laplaza, R.; Das, S.; Wodrich, M. D.; Corminboeuf, C. Constructing and interpreting volcano plots and activity maps to navigate homogeneous catalyst landscapes. *Nat. Protoc.* **2022**, *17*, 2550−2569.

(45) Ryu, H.; Park, J.; Kim, H. K.; Park, J. Y.; Kim, S.-T.; Baik, M.-H. Pitfalls in Computational Modeling of Chemical Reactions and How To Avoid Them. *Organometallics* **2018**, *37*, 3228−3239.

(46) Harvey, J. N.; Himo, F.; Maseras, F.; Perrin, L. Scope and Challenge of Computational Methods for Studying Mechanism and Reactivity in Homogeneous Catalysis. *ACS Catal.* **2019**, *9*, 6803−6813.

(47) Fey, N.; Lynam, J. M. Computational mechanistic study in organometallic catalysis: Why prediction is still a challenge. *Wiley Interdiscip. Rev.: Comput. Mol. Sci.* **2022**, *12*, e1590.

(48) Meek, S. J.; Pitman, C. L.; Miller, A. J. M. Deducing Reaction Mechanism: A Guide for Students, Researchers, and Instructors. *J. Chem. Educ.* **2016**, *93*, 275−286.

(49) Eyring, H. The Activated Complex in Chemical Reactions. *J. Chem. Phys.* **1935**, *3*, 107−115.

(50) Virtanen, P.; Gommers, R.; Oliphant, T. E.; et al. SciPy 1.0: fundamental algorithms for scientific computing in Python. *Nat. Methods* **2020**, *17*, 261−272.

(51) Maclaurin, D.; Duvenaud, D.; Adams, R. P. In *Autograd: Effortless gradients in numpy*, ICML 2015 AutoML Workshop, 2015; p 5.

(52) Savitzky, A.; Golay, M. J. E. Smoothing and Differentiation of Data by Simplified Least Squares Procedures. *Anal. Chem.* **1964**, *36*, 1627−1639.

(53) Boulfelfel, D.; Rangayyan, R.; Hahn, L.; Kloiber, R. Three-dimensional restoration of single photon emission computed tomography images. *IEEE Trans. Nucl. Sci.* **1994**, *41*, 1746−1754.

(54) Franke, R.; Selent, D.; Börner, A. Applied Hydroformylation. *Chem. Rev.* **2012**, *112*, 5675−5732.

(55) Somasunderam, A.; Alper, H. Use of rhodium on carbon and 1, 3-bis(diphenylphosphino)propane to catalyze the regioselective hydroformylation of alkenes with formic acid as the hydrogen source. *J. Mol. Catal.* **1994**, *92*, 35−40.

(56) Vilches-Herrera, M.; Concha-Puelles, M.; Carvajal, N.; Molina, J.; Santander, R.; Caroli Rezende, M.; Lühr, S. Influence of the bite natural angle of bidentate diphosphine ligands in the syngas-free branched hydroformylation of $\beta$-functionalized olefins. *Catal. Commun.* **2018**, *116*, 62−66.

(57) Casey, C. P.; Paulsen, E. L.; Beuttenmueller, E. W.; Proft, B. R.; Matter, B. A.; Powell, D. R. Electronically Dissymmetric DIPHOS Derivatives Give Higher n:i Regioselectivity in Rhodium-Catalyzed Hydroformylation Than Either of Their Symmetric Counterparts. *J. Am. Chem. Soc.* **1999**, *121*, 63−70.

(58) Ibrahim, M. Y.; Bennett, J. A.; Mason, D.; Rodgers, J.; Abolhasani, M. Flexible homogeneous hydroformylation: on-demand tuning of aldehyde branching with a cyclic fluorophosphite ligand. *J. Catal.* **2022**, *409*, 105−117.

(59) Free energy corrections, which are included in the relative free energies of the species in the catalytic cycle, depend on temperature. This may potentially alter the energy barriers and rate constants. We do not account for the temperature dependence of free energy corrections here since in this case (see Figure S4) energy barriers remain constant with temperature in the 280−400 K range.

(60) Keulemans, A. I. M.; Kwantes, A.; van Bavel, T. The structure of the formylation (OXO) products obtained from olefines and watergas. *Recl. Trav. Chim. Pays-Bas* **1948**, *67*, 298−308.

(61) Adamo, C.; Barone, V. Toward reliable density functional methods without adjustable parameters: The PBE0 model. *J. Chem. Phys.* **1999**, *110*, 6158−6170.

(62) Perdew, J. P.; Burke, K.; Ernzerhof, M. Generalized Gradient Approximation Made Simple. *Phys. Rev. Lett.* **1996**, *77*, 3865−3868.

(63) Steinmann, S. N.; Corminboeuf, C. A System-Dependent Density-Based Dispersion Correction. *J. Chem. Theory Comput.* **2010**, *6*, 1990−2001.

(64) Steinmann, S. N.; Corminboeuf, C. Comprehensive Benchmarking of a Density-Dependent Dispersion Correction. *J. Chem. Theory Comput.* **2011**, *7*, 3567−3577.

(65) Steinmann, S. N.; Corminboeuf, C. A density dependent dispersion correction. *Chimia* **2011**, *65*, 240−244.

(66) Steinmann, S. N.; Corminboeuf, C. A generalized-gradient approximation exchange hole model for dispersion coefficients. *J. Chem. Phys.* **2011**, *134*, No. 044117.

(67) Zhao, Y.; Truhlar, D. G. The M06 suite of density functionals for main group thermochemistry, thermochemical kinetics, non-covalent interactions, excited states, and transition elements: two new functionals and systematic testing of four M06-class functionals and 12 other functionals. *Theor. Chem. Acc.* **2008**, *120*, 215−241.

(68) Weigend, F.; Ahlrichs, R. Balanced basis sets of split valence, triple zeta valence and quadruple zeta valence quality for H to Rn: Design and assessment of accuracy. *Phys. Chem. Chem. Phys.* **2005**, *7*, 3297−3305.

(69) Frisch, M. J.; et al. *Gaussian 09*, revision A.1; Gaussian Inc.: Wallingford, CT, 2009.

(70) te Velde, G.; Bickelhaupt, F. M.; Baerends, E. J.; Fonseca Guerra, C.; van Gisbergen, S. J. A.; Snijders, J. G.; Ziegler, T. Chemistry with ADF. *J. Comput. Chem.* **2001**, *22*, 931−967.

(71) Steinmann, S. N.; Corminboeuf, C. A System-Dependent Density-Based Dispersion Correction. *J. Chem. Theory Comput.* **2010**, *6*, 1990−2001.

(72) Klamt, A. The COSMO and COSMO-RS solvation models. *Wiley Interdiscip. Rev.: Comput. Mol. Sci.* **2011**, *1*, 699−709.

(73) Rappoport, D.; Furche, F. Property-optimized Gaussian basis sets for molecular response calculations. *J. Chem. Phys.* **2010**, *133*, 134105.

(74) Frisch, M. J.; et al. *Gaussian 16*, revision C.01; Gaussian Inc.: Wallingford, CT, 2016.